

Kineticomechanistic Study of the Redox pH Cycling Processes Occurring on a Robust Water-Soluble Cyanido-Bridged Mixed-Valence $\{\text{Co}^{\text{III}}/\text{Fe}^{\text{II}}\}_2$ Square

Laura Alcázar,[†] Paul V. Bernhardt,[‡] Montserrat Ferrer,[†] Mercè Font-Bardia,[§] Albert Gallen,[†] Jesús Jover,[†] Manuel Martínez,^{*,†} Jack Peters,[†] and Timothy J. Zerk[‡]

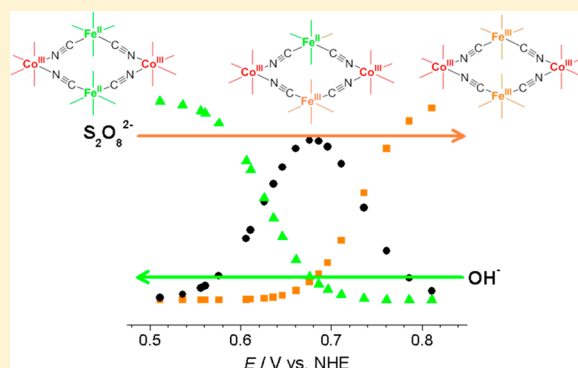
[†]Departament de Química Inorgànica i Orgànica, Secció de Química Inorgànica, Universitat de Barcelona, Martí i Franquès 1–11, E-08028 Barcelona, Spain

[‡]School of Chemistry and Molecular Biosciences, University of Queensland, Brisbane 4072, Queensland, Australia

[§]Unitat de Difracció de RX, Centres Científics i Tecnològics de la Universitat de Barcelona, Universitat de Barcelona, Solé i Sabarís 1–3, E-08028 Barcelona, Spain

Supporting Information

ABSTRACT: A kineticomechanistic study of reversible electron-transfer processes undergone by the water-soluble, cyanido-bridged mixed-valence $[\{\text{Co}^{\text{III}}\{(\text{Me})_2(\mu\text{-ET})\text{cyclen}\}\}_2\{(\mu\text{-NC})_2\text{Fe}^{\text{II}}(\text{CN})_4\}_2]^{2-}$ square has been carried out. The oxidation reaction consists of a two-step process with the participation of a solvent-assisted outer-sphere complex, as a result of the establishment of hydrogen bonds that involve the oxo groups of the oxidant (peroxodisulfate) and the terminal cyanido ligands of the tetrametallic square. The formally endergonic reduction reaction of the fully oxidized $([\{\text{Co}^{\text{III}}\{(\text{Me})_2(\mu\text{-ET})\text{cyclen}\}\}_2\{(\mu\text{-NC})_2\text{Fe}^{\text{III}}(\text{CN})_4\}_2])$ core by water, producing hydrogen peroxide from water even at low pH values, is also a two-step process. Each one of these processes requires a set of two preequilibria involving the association of OH^- and its subsequent deprotonation by a further OH^- anion. The structure of the square compound in its fully protonated form has also been determined by X-ray diffraction and shows the existence of strong hydrogen-bonding interactions, in agreement with the rather high basicity of the terminal cyanido ligands. Likewise, density functional theory calculations on the tetrametallic complex showed zones with negative electrostatic potential around the Fe^{II} centers of the square that would account for the establishment of the hydrogen bonds found in the solid state. Spectroelectrochemistry experiments demonstrated the singular stability of the $\{\text{Co}^{\text{III}}/\text{Fe}^{\text{II}}\}_2^{2-}$ complex, as well as that of their partially, $\{\text{Co}_2^{\text{III}}/\text{Fe}^{\text{III}}\text{Fe}^{\text{II}}\}^-$, and fully, $\{\text{Co}^{\text{III}}/\text{Fe}^{\text{III}}\}_2$, oxidized counterparts because no hysteresis was observed in these measurements.



INTRODUCTION

Self-assembly of macrocyclic metal complexes is a powerful method for the construction of well-defined architectures with interesting structure-specific properties such as guest recognition, optical and/or magnetic properties, or multiredox behavior among many others.^{1–3} Given the fact that a large variety of metallamacrocycles are built with redox-active transition-metal fragments as corners and/or redox-active ligands as linkers, it is rather surprising that the number of studies that specifically aim at taking advantage of that inherent property is still rather limited. Nevertheless, in recent years, there has been a growing interest in these redox-active species because of their potentially useful properties (optical, magnetic, and catalytic activity, molecular recognition, etc.). Published comprehensive reports^{4,5} provide examples of electroactive metallic assemblies whose redox activity is localized in the organic ligands and/or metallic corners.

Although the number of examples containing redox-active bridging ligands (based on units such as tetrathiafulvalene or perylene bisimide) or blocking ligands (bearing moieties such as ferrocenyl) is much larger than that including redox-active metal corners, some macrocycles containing $\text{Cu}^{\text{II}}/\text{Cu}^{\text{III}}$, $\text{Co}^{\text{II}}/\text{Co}^{\text{III}}$, $\text{Co}^{\text{III}}/\text{Co}^{\text{IV}}$, $\text{Fe}^{\text{II}}/\text{Fe}^{\text{III}}$, $\text{Ru}^{\text{II}}/\text{Ru}^{\text{III}}$, or $\text{Mo}^{\text{II}}/\text{Mo}^{\text{III}}$ as redox-active pairs have been reported.^{6–10} Surprisingly, these reports lack any reference to discrete cyanido-bridged (Prussian blue) species, although these compounds usually display redox activity because of the presence of multiple Fe and/or Co oxidation states.¹¹ Nevertheless, an increasing number of interesting examples of Prussian blue molecular polymetallic assemblies have been reported because of the fact that they usually exhibit both optical and magnetic bistability, which arises from a reversible metal-to-metal charge transfer between

Received: April 27, 2018

Scheme 1. Mechanistic Process Involved in the Preparation of the Cyanido-Bridged $[\{\text{Co}^{\text{III}}\{(\text{Me})_2(\mu\text{-ET})\text{cyclen}\}\}_2\{(\mu\text{-NC})_2\text{Fe}^{\text{II}}(\text{CN})_4\}]^{2-}$ Square Complex of This Study

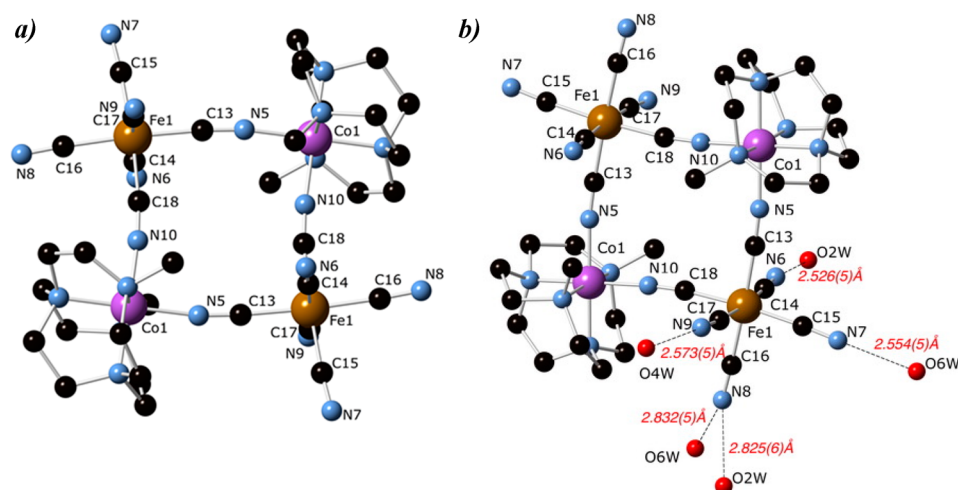
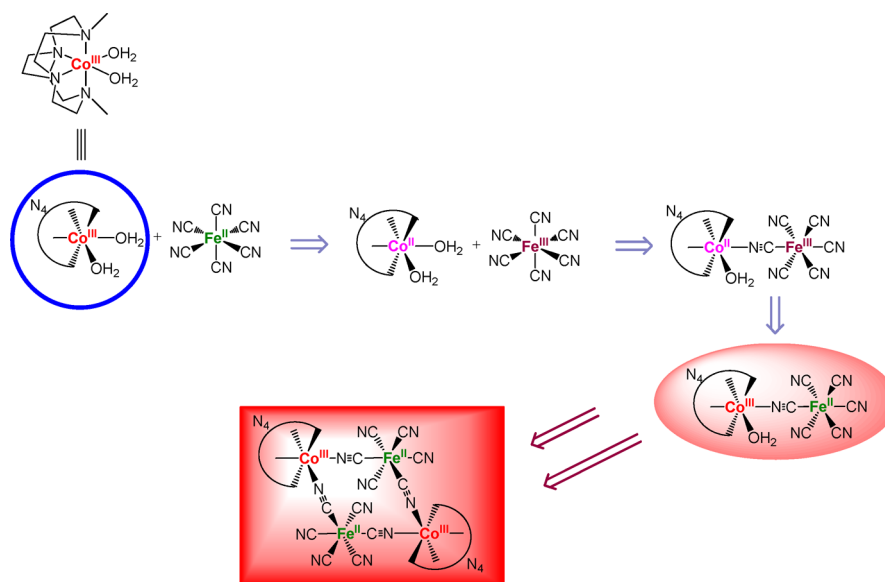


Figure 1. X-ray crystal structure of $(\text{H}_3\text{O})_6[\{\text{Co}^{\text{III}}\{(\text{Me})_2(\mu\text{-ET})\text{cyclen}\}\}_2\{(\mu\text{-NC})_2\text{Fe}^{\text{II}}(\text{CN})_4\}] \cdot (\text{ClO}_4)_4 \cdot 4\text{H}_2\text{O}$. (a) Square unit of the mixed-valence complex. The H atoms, solvent, and counterions are omitted for clarity. Selected bond lengths (Å) and angles (deg): Co1–N10 1.909(3), Co1–N5 1.918(3), Co1–N2 1.925(3), Co1–N3 1.935(3), Co1–N4 1.982(3), Co1–N1 1.989(3), Fe1–C17 1.880(4), Fe1–C14 1.885(4), Fe1–C15 1.896(4), Fe1–C18 1.902(4), Fe1–C13 1.910(4), Fe1–C16 1.921(4); N10–Co1–N5 88.81(13), C18–Fe1–C13 90.49(15), C18–N10–Co1 173.1(3), N10–C18–Fe1 173.5(3), C13–N5–Co1 171.7(3), N5–C13–Fe1 176.0(3). (b) Part of the extensive 3D network found in the structure, showing the variety of hydrogen-bond lengths.

the Co^{III} (or Fe^{III}) and Fe^{II} centers. This family of compounds includes pentanuclear trigonal-bipyramidal $\{\text{Fe}^{\text{II}}_2/\text{Fe}^{\text{III}}_3\}$ and $\{\text{Fe}^{\text{II}}_2/\text{Co}^{\text{III}}_3\}$ units,^{12,13} octanuclear cubic $\{\text{Fe}^{\text{II}}/\text{Fe}^{\text{III}}\}_4$ and $\{\text{Fe}^{\text{II}}/\text{Co}^{\text{III}}\}_4$ assemblies,^{14,15} homonuclear $\{\text{Fe}^{\text{II}}/\text{Fe}^{\text{III}}\}_2$ squares,^{16,17} and a significant number of heterotetranuclear square complexes $\{\text{Fe}^{\text{II}}/\text{Co}^{\text{III}}\}_2$.^{11,18–25} Recently, we have reported the preparation of the diamagnetic cyanido-bridged $[\{\text{Co}^{\text{III}}\{(\text{Me})_2(\mu\text{-ET})\text{cyclen}\}\}_2\{(\mu\text{-NC})_2\text{Fe}^{\text{II}}(\text{CN})_4\}]^{2-}$ square complex²⁶ via a mechanistically designed, self-assembly reaction (Scheme 1). The process involves a rate-limiting outer-sphere redox reaction, followed by a fast substitution/inner-sphere redox reaction, sequence that had been studied by us for some time.^{27–34} Although this compound did not show any evidence of complete intramolecular electron-transfer phenomena, its striking stability in aqueous solution (stable

across the full aqueous pH range, in deep contrast with that of other reported redox-active metallomacrocycles) opens up the possibility of performing a thorough study of its participation in chemical processes, such as reversible oxidation, protonation, and OH^- association.

With these facts in mind, we are here reporting a redox-reversible kineticomechanistic study of this tetrametallic $\{\text{Co}^{\text{III}}/\text{Fe}^{\text{II}}\}_2$ unit as a function of pH, oxidant concentration, temperature, and pressure. In addition, a study of the charge distribution of the fully reduced species and the one- and two-electron oxidized forms by density functional theory (DFT) calculations has been carried out in order to rationalize our experimental observations. The results indicate an extreme robustness of the square unit across the aqueous pH range, as well as a significant contribution from specific outer-sphere

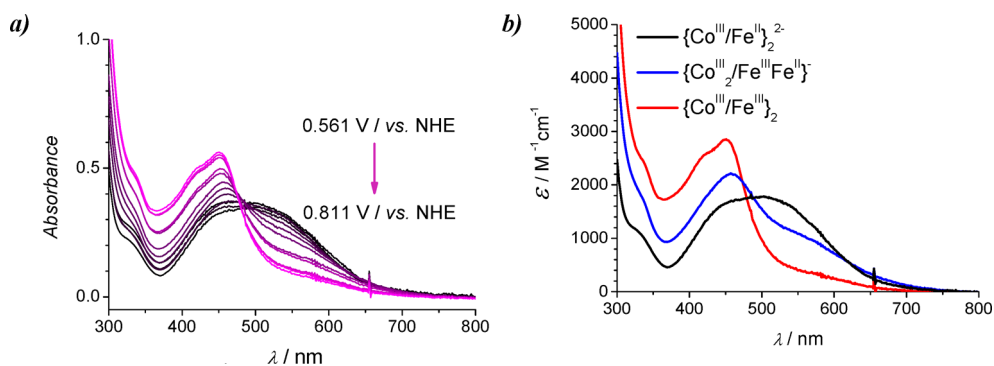


Figure 2. (a) Spectroelectrochemistry of a 2.0×10^{-3} M solution of $\{\text{Co}^{\text{III}}/\text{Fe}^{\text{II}}\}_2^{2-}$ in H_2O (pH 7 and $I = 0.1$ M LiClO_4). A platinum flag working electrode, an $\text{Ag}/\text{AgCl}/\text{saturated NaCl}$ reference electrode, and a platinum wire counter electrode were used. Cell path length = 1.0 mm. (b) ReactLab-calculated spectra of the fully oxidized $\{\text{Co}^{\text{III}}/\text{Fe}^{\text{III}}\}_2$, fully reduced $\{\text{Co}^{\text{III}}/\text{Fe}^{\text{II}}\}_2^{2-}$, and intermediate $\{\text{Co}^{\text{III}}/\text{Fe}^{\text{III}}\text{Fe}^{\text{II}}\}^-$ complexes [aqueous solution, pH 7, $I = 0.1$ M LiClO_4 , $E_{\text{Fe}^{\text{II}}/\text{Fe}^{\text{III}}(1)} = 0.628$ V, and $E_{\text{Fe}^{\text{II}}/\text{Fe}^{\text{III}}(2)} = 0.7322$ V vs NHE].

recognition of water molecules, which actuate in a way that cannot be attributed to mere electrostatic effects. These features allow consideration of the complexes studied as having a versatile multiredox chemistry with implications in electrochromism.

RESULTS AND DISCUSSION

Crystal Structure of $(\text{H}_3\text{O})_6\{\{\text{Co}^{\text{III}}\{(\text{Me})_2(\mu\text{-ET})\text{cyclen}\}\}_2\{(\mu\text{-NC})_2\text{Fe}^{\text{II}}(\text{CN})_4\}_2\} \cdot (\text{ClO}_4)_4 \cdot 4\text{H}_2\text{O}$. Even though the central core of the title compound has already been inferred via several techniques,²⁶ its crystal structure was unknown. Nevertheless, knowledge of the protonation and redox properties of the compound has enabled us to design a way to produce it in a form that could be crystallized.

Caramel-colored crystals of the title complex were obtained by slow concentration of a 1 M HClO_4 solution of the parent compound $\text{Na}_2[\{\{\text{Co}^{\text{III}}\{(\text{Me})_2(\mu\text{-ET})\text{cyclen}\}\}_2\{(\mu\text{-NC})_2\text{Fe}^{\text{II}}(\text{CN})_4\}_2\}]$ at 4°C . The structure contains centrosymmetric cyanido-bridged $\{\text{Fe}_2(\mu\text{-CN})_4\text{Co}_2\}$ units bearing a nearly planar, square-shaped geometry, in which the Co and Fe ions are bridged by cyanide ions. The anion structure, together with selected bond distances and bond angles, is shown in Figure 1a.

The distances between adjacent Fe and Co centers through the cyanide linkers are very similar [4.936(2) and 4.956(2) Å], and the angles Fe1-Co1-Fe1 and Co1-Fe1-Co1 are 88.47(1) and 91.53(1)°, respectively, thus displaying a regular square macrocyclic core, in good agreement with other reported examples of squares containing $\{\text{Co}^{\text{III}}\text{-NC-Fe}^{\text{II}}\}$ edges.^{18,20,35} The coordination bond lengths about the Co ion are in the range of 1.909(3)–1.989(3) Å, characteristic of low-spin (LS) Co^{III} ions.¹² The Fe–C distances are within 1.880(4) and 1.921(4) Å, confirming the LS character of the Fe ions present in the compound and its divalent oxidation state.²³ The total compound charge, as well as the absence of a ligand-to-metal charge-transfer (LMCT; $\text{Fe}^{\text{III}}\text{-CN}$) band near 400 nm (characteristic of the ferricyanide chromophore) in the electronic spectrum, is in agreement with the Fe^{II} centers in the complex.

In addition to the discrete tetranuclear metal units $[\{\{\text{Co}^{\text{III}}\{(\text{Me})_2(\mu\text{-ET})\text{cyclen}\}\}_2\{(\mu\text{-NC})_2\text{Fe}^{\text{II}}(\text{CN})_4\}_2\}]^{2-}$, perchlorate anions, hydronium cations, and lattice H_2O molecules are also found in the asymmetric unit. The anionic squares are stacked, forming columns along the b axis (Figure S1) with an angle of 57.4° between the planes of consecutive macrocycles.

Moreover, a complex 3D network is formed as a result of the establishment of extensive hydrogen-bonding interactions that involve the O atoms of the H_2O molecules, H_3O^+ cations, and ClO_4^- anions and the N atoms of all terminal cyanido ligands (Figure 1b). Interestingly, three of these interactions are singularly strong [$\text{O2W}\cdots\text{N6} = 2.525(5)$ Å, $\text{O6W}\cdots\text{N7} = 2.554(5)$ Å, and $\text{O4W}\cdots\text{N9} = 2.573(5)$ Å] in comparison with those reported for analogous square $\{\text{Co}^{\text{III}}\text{Fe}^{\text{II}}\}_2$ compounds,^{20,24,37} in agreement with the basic character exhibited by the terminal CN groups of the compound.

Spectroelectrochemistry: Redox Stability. We previously measured the cyclic voltammetry of the title complex in an aqueous solution and showed that it exhibits two discrete $\text{Fe}^{\text{III/II}}$ redox couples.²⁶ Both $\text{Fe}^{\text{III/II}}$ redox couples are reversible, which indicates that the complex is stable in each of the fully oxidized $\text{Fe}^{\text{III}}\text{Fe}^{\text{III}}$, fully reduced $\text{Fe}^{\text{II}}\text{Fe}^{\text{II}}$, and intermediate $\text{Fe}^{\text{III}}\text{Fe}^{\text{II}}$ forms, while the $\text{Co}^{\text{III/II}}$ redox couples are irreversible under the same conditions. Herein we measured the spectroelectrochemistry of the complex at pH 7, poisoning the potential at increasingly positive potentials (oxidation) and then returning incrementally to the starting potential (reduction). At each poised potential, the observed spectrum was stable for a minimum of 1 h, and no hysteresis was observed in the spectra of the oxidation and reduction sweeps (Figure S2), which testifies to the stability of the complex. Modeling the data from Figure 2a using ReactLab Redox³⁶ revealed the spectrum of the intermediate $\text{Fe}^{\text{III}}\text{Fe}^{\text{II}}$ complex (Figure 2b, blue curve). The separation of the two $\text{Fe}^{\text{III/II}}$ couples ($\Delta E > 100$ mV) is much larger than that expected for two noninteracting Fe centers ($2RT/F \ln 2 = 35.6$ mV),³⁸ which shows that the charge increase at one oxidized Fe center influences the redox potential of the other Fe center, thus raising its redox potential.

DFT Calculations. In view of the feasibility of pursuing the kinetic/mechanistic studies of the reversible redox processes indicated in Figure 2 and given the fact that the $\{\text{Co}^{\text{III}}/\text{Fe}^{\text{II}}\}_2^{2-}$ core is extremely robust, DFT calculations have been conducted in order to investigate the possible differences among the $\{\text{Co}^{\text{III}}/\text{Fe}^{\text{II}}\}_2^{2-}/\{\text{Co}^{\text{III}}_2/\text{Fe}^{\text{III}}\text{Fe}^{\text{II}}\}^-/\{\text{Co}^{\text{III}}/\text{Fe}^{\text{III}}\}_2$ triad that could explain the reactivity observed.

These structures were optimized with DFT calculations using the crystal structure of the $\{\text{Co}^{\text{III}}/\text{Fe}^{\text{II}}\}_2^{2-}$ core as the starting point (the detailed procedure is described in the Experimental Section). From the calculations, the oxidation process does not entail major changes in the structure; the

central square unit of the $\{\text{Co}^{\text{III}}\text{Fe}^{\text{II}}\}_2^{2-}$ complex remains practically the same, with Fe...Co, Fe...Fe, and Co...Co distances of 4.99, 6.93, and 7.20 Å, respectively. These values are very similar to those found in the crystal structure, where the average Fe...Co separation is 4.95 Å, while the Fe...Fe and Co...Co distances are 6.90 and 7.09 Å. In the same line, the computed Fe...Co...Fe and Co...Fe...Co angles are close to those in the crystal structure: 87.8 versus 88.5° and 92.2 versus 91.5°, respectively. In all cases, as in the determined crystal structure, the four metals remain in the same plane and the octahedral $\text{Fe}(\text{CN})_6$ units show an eclipsed arrangement, with twist angles between the iron hexacyanido units always below 0.5°. The consecutive oxidation of the $\{\text{Co}^{\text{III}}\text{Fe}^{\text{II}}\}_2^{2-}$ complex produces open-shell species with one unpaired electron in the oxidized Fe centers. For the half-oxidized $\{\text{Co}^{\text{III}}_2/\text{Fe}^{\text{III}}\text{Fe}^{\text{II}}\}^-$ species, the unpaired electron is localized on the new Fe^{III} center (Figure 3a), while for the fully oxidized $\{\text{Co}^{\text{III}}/\text{Fe}^{\text{III}}\}_2$

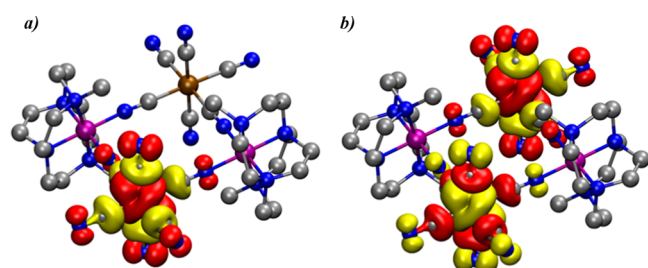


Figure 3. Electron spin densities computed for complexes (a) $\{\text{Co}^{\text{III}}/\text{Fe}^{\text{III}}\}_2^-$ and (b) $\{\text{Co}^{\text{III}}/\text{Fe}^{\text{III}}\}_2$. Color code: C, gray; N, blue; Fe, brown; Co, purple. H atoms have been omitted for clarity.

complex, the species can be either a triplet or an open-shell singlet; in practice, both possibilities have practically the same energy and display very similar structures. All of the results appearing throughout this manuscript refer to the open-shell singlet $\{\text{Co}^{\text{III}}/\text{Fe}^{\text{III}}\}_2$ complex. As in the $\{\text{Co}^{\text{III}}_2/\text{Fe}^{\text{II}}\text{Fe}^{\text{III}}\}^-$ species, the electron spin density remains localized on the Fe^{III} centers (Figure 3b).

The molecular electrostatic potential (MEP) maps show the formal charge distribution of the total electron density of the complexes, i.e., the regions with charge depletion and accumulation that can be used to explain the reactivity and outer sphere interactions (Figure 4). As expected, the positively charged areas are always located around the Co centers, while the Fe surroundings are more negative in all species. The maximum and minimum surface charge values vary according to the total charge of the complexes, i.e., red-to-

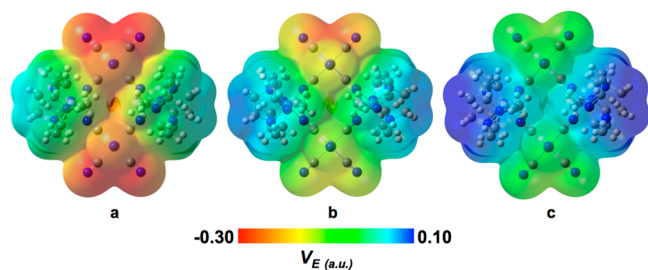


Figure 4. MEP maps on the 0.002 isosurfaces of (a) $\{\text{Co}^{\text{III}}\text{Fe}^{\text{II}}\}_2^{2-}$, (b) $\{\text{Co}^{\text{III}}_2/\text{Fe}^{\text{III}}\text{Fe}^{\text{II}}\}^-$, and (c) $\{\text{Co}^{\text{III}}/\text{Fe}^{\text{III}}\}_2$. Red and blue colors represent negative and positive values of the electrostatic potential (V_E).

light-blue surface for $\{\text{Co}^{\text{III}}/\text{Fe}^{\text{II}}\}_2^{2-}$, orange-to-blue surface for $\{\text{Co}^{\text{III}}_2/\text{Fe}^{\text{III}}\text{Fe}^{\text{II}}\}^-$, and green-to-dark-blue surface for $\{\text{Co}^{\text{III}}/\text{Fe}^{\text{III}}\}_2$ in Figure 4. The MEP map of $\{\text{Co}^{\text{III}}/\text{Fe}^{\text{II}}\}_2^{2-}$ clearly reflects the bonding found in the crystal structure, where the square tetrametallic core interacts with H_3O^+ through hydrogen bonding of the terminal, negatively charged, cyanido ligands bound to the Fe centers. The different Fe^{II} and Fe^{III} atoms in $\{\text{Co}^{\text{III}}_2/\text{Fe}^{\text{III}}\text{Fe}^{\text{II}}\}^-$ can be clearly distinguished with the MEP map; the former is located in a zone with negative electrostatic potential (orange, Figure 4b, top), while the latter belongs to a space where the surface charge is more positive (yellow, Figure 4b, bottom).

The $\{\text{Co}^{\text{III}}/\text{Fe}^{\text{III}}\}_2$ complex reacts with hydroxide to produce hydrogen peroxide (H_2O_2) and the reduced $\{\text{Co}^{\text{III}}/\text{Fe}^{\text{II}}\}_2^{2-}$ species (see below). The experimental data indicate that this is an outer-sphere redox process. Nevertheless, the small size of the OH^- anion could suggest an encapsulation of the anion in the central cavity of the tetranuclear metallic core prior to electron transfer. This hypothesis has been tested by optimizing a $\{\text{Co}^{\text{III}}/\text{Fe}^{\text{III}}\}_2\text{OH}^-$ species in which the hydroxide anion is placed in the geometrical center of the cavity. After optimization, the hydroxide group is observed to migrate to the external part of the complex, where it can interact with the dangling methyl groups of the cyclen ligand. Because the metal centers surrounding the cavity do not exert any stabilizing effect on the incoming OH^- group, a mechanism where the hydroxo groups are inside the cavity would not be expected.

Kinetics of the Oxidation Reaction of the $\{\text{Co}^{\text{III}}/\text{Fe}^{\text{II}}\}_2^{2-}$ Complex. The oxidation reaction of simpler but related $(\text{Co}^{\text{III}}/\text{Fe}^{\text{II}})^-$ mixed-valence dinuclear complexes, sodium μ -cyanido- $1\kappa\text{N}:2\kappa\text{C}$ -(2-methyltetraazacycloamine)- $1\kappa^5\text{N}$ -penta-cyanido- $2\kappa^5\text{C}$ -[1-cobalt(III)-1-ferrate(II)], with peroxodisulfate has been already studied, and the behavior has been explained as an initial one-electron oxidation of Fe^{II} to Fe^{III} producing SO_4^{2-} and $\text{SO}_4^{\bullet-}$, followed by a fast (non-rate-determining) second one-electron process involving the $\text{SO}_4^{\bullet-}$ radical.^{30,34,39,40} In view of the spectroelectrochemical data shown above, as well as the redox nonequivalence of the two Fe centers,²⁶ the oxidation of the new $\{\text{Co}^{\text{III}}/\text{Fe}^{\text{II}}\}_2^{2-}$ mixed-valence square was pursued from a kineticomechanistic perspective at varying concentrations of peroxodisulfate, pH, temperature, and pressure. As collected in Table S1, in all cases the time-resolved spectra agree with the operation of a two-step consecutive process in the acidity range between pH 8.5 and 1 M HClO_4 . Furthermore, the *Specfit*- or *ReactLab*-Kinetics calculated spectra^{41,42} of the intermediate compound agree with that of the single-electron-oxidized $\{\text{Co}^{\text{III}}_2/\text{Fe}^{\text{III}}\text{Fe}^{\text{II}}\}^-$ mixed-valence compound determined from the spectroelectrochemical measurements (see Figures 2 and S3). Figure 5 collects an example of the trends observed for the two pseudo-first-order rate constants derived (k_{obs1} and k_{obs2}) with the concentration of the oxidant.

By a comparison with our previous data on the $(\text{Co}^{\text{III}}/\text{Fe}^{\text{II}})$ dinuclear complexes, the reaction can be explained by the sequence shown in Scheme 2, which produces a rate law such as that indicated in eq 1 for both rate-determining reaction steps.^{43–45} Nevertheless, it is clear that for the observation of the second step in the reaction sequence (ox2a and ox2b), the $\text{SO}_4^{\bullet-}$ radical generated by the first oxidation step (ox1a and ox1b) has to react preferentially with an excess of the reducing $\{\text{Co}^{\text{III}}/\text{Fe}^{\text{II}}\}_2^{2-}$ to further produce the $\{\text{Co}^{\text{III}}_2/\text{Fe}^{\text{III}}\text{Fe}^{\text{II}}\}^-$ intermediate (oxf1). Any other option would make the

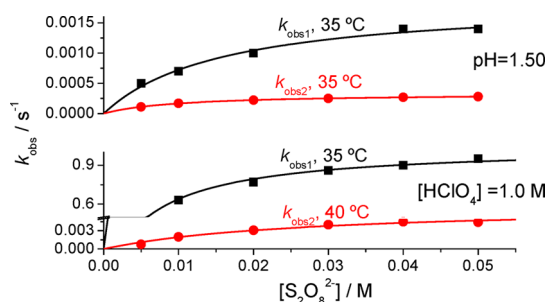
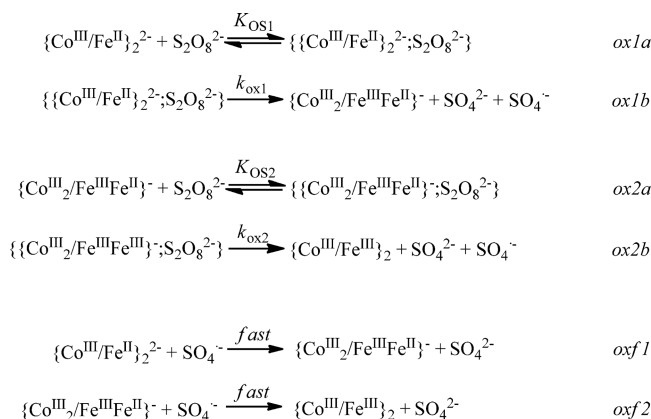


Figure 5. Plot of the values of the first-order rate constants, k_{obs} , for the two-step $\text{S}_2\text{O}_8^{2-}$ oxidation of the $\{\text{Co}^{\text{III}}/\text{Fe}^{\text{II}}\}_2^{2-}$ mixed-valence square at different temperatures and acidities.

Scheme 2



reaction sequence show a single rate-determining step behavior.

$$k_{\text{obs}} = \frac{k_{\text{ox}}K_{\text{OS}}[\text{S}_2\text{O}_8^{2-}]}{1 + K_{\text{OS}}[\text{S}_2\text{O}_8^{2-}]} \quad (1)$$

From the curvature shown in the plots, it is clear that both k_{obs} rate constants show the typical limiting behavior obtained for outer-sphere redox processes, where the formation of the precursor outer-sphere complex (K_{OS}) is dominant.⁴⁴ Although this effect had not previously been observed for oxidations by $\text{S}_2\text{O}_8^{2-}$, the reaction of the dinuclear $(\text{Co}^{\text{III}}/\text{Fe}^{\text{II}})^-$ species with $[\text{Co}^{\text{III}}(\text{oxalate})_3]^{3-}$ effectively showed this behavior. Important interactions in the outer-sphere precursor complex had been established as responsible of this fact.^{29,40}

From the limiting value obtained from fitting the data to eq 1, the values of k_{ox} and K_{OS} at different temperatures and pH can be derived for both reaction steps (ox1 and ox2, Scheme 2). By measurement of the temperature dependence of k_{ox} and fitting the data to the Eyring equation (Figure 6a), the corresponding thermal activation parameters can be calculated for both electron-transfer processes. The pressure dependence of the values of k_{obs} at concentrations of $\text{S}_2\text{O}_8^{2-}$ at which the plot has practically reached saturation ($k_{\text{ox}} \approx k_{\text{obs}}$ at $[\text{S}_2\text{O}_8^{2-}] = 0.05\text{--}0.07\text{ M}$) was also studied in order to determine the activation volumes of the two steps. Figure 6b shows some of the $\ln k_{\text{ox}}$ versus P plots at the pH where a definite neat oxidation is observed (see the next section),⁴⁶ and Table 1 collects a summary of the equilibrium kinetic and activation data determined.

Kinetics of the $\{\text{Co}^{\text{III}}/\text{Fe}^{\text{III}}\}_2$ Complex Reduction. From our previous studies carried out on the simpler $(\text{Co}^{\text{III}}/\text{Fe}^{\text{II}})^-$ mixed-valence dinuclear complexes, a pH-dependent reversible redox process has been demonstrated.^{30,40} Consequently, the reduction process of the new $\{\text{Co}^{\text{III}}/\text{Fe}^{\text{III}}\}_2$ square (obtained by peroxodisulfate oxidation in the acidic conditions of $\{\text{Co}^{\text{III}}/\text{Fe}^{\text{II}}\}_2^{2-}$)²⁶ in alkaline solutions to produce H_2O_2 was also studied from a kineticomechanistic perspective. As indicated in the Experimental Section, the presence of H_2O_2 in the final reaction mixture was confirmed by standard peroxide test kits; no reaction of the parent $\{\text{Co}^{\text{III}}/\text{Fe}^{\text{II}}\}_2^{2-}$ square with H_2O_2 has been observed with excesses of up to 100-fold. Interestingly, for this new tetranuclear $\{\text{Co}^{\text{III}}/\text{Fe}^{\text{III}}\}_2$ compound, the reduction process reverting to the mixed-valence $\{\text{Co}^{\text{III}}/\text{Fe}^{\text{II}}\}_2^{2-}$ square complex, with the formation of H_2O_2 , is observed even at acidic pH values (the reaction is observed from pH 3 upward). As found for the previously described oxidation reaction by peroxodisulfate, the reduction process is clearly a consecutive two-step sequence from the time-resolved fitting of the full spectra by the standard software indicated in the Experimental Section.^{42,43}

Figure 7 summarizes the trends observed for the values of $k_{\text{obs}1}$ and $k_{\text{obs}2}$ with the concentration of OH^- . For the reduction of the simpler $(\text{Co}^{\text{III}}/\text{Fe}^{\text{III}})^-$ dinuclear complexes, two equilibrium processes involving the OH^- reductant precede the rate-determining formation of peroxide; these are the formation of an OH^- adduct, followed by its deprotonation by another OH^- . Thus, an $[\text{OH}^-]^2$ dependence of the k_{obs} rate constants is observed.⁴⁰ In the present case, this is not so, and a double titration plot is observed with $\text{p}K_{\text{eq}}$ values within the 3–4 and 11–12 ranges. Table S2 collects all

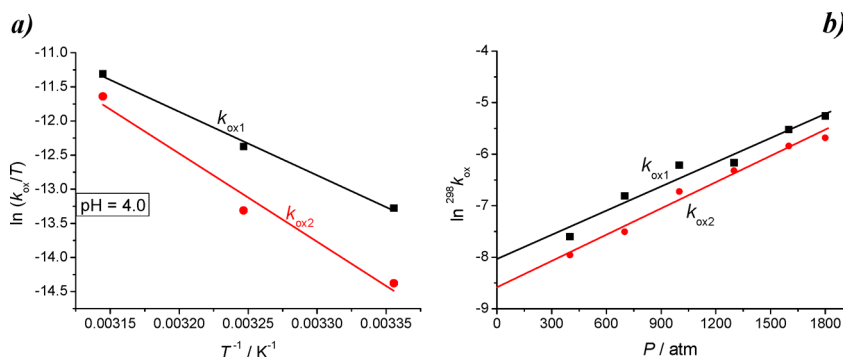


Figure 6. (a) Eyring plot for variation of the values of k_{ox} for the two steps observed with the temperature at pH 4.0. (b) $\ln k_{\text{ox}}$ versus P plot for the reaction carried out at pH 2.0 and 25 °C.

Table 1. Thermal and Pressure Activation Parameters for the Two Consecutive Reaction Steps Observed in the Oxidation of the $\{\text{Co}^{\text{III}}/\text{Fe}^{\text{II}}\}_2^{2-}$ Mixed-Valence Square with $\text{S}_2\text{O}_8^{2-}$ at Different pH Values^a

pH	$K_{\text{OS1}}/\text{M}^{-1}$	$^{298}k_{\text{ox1}}/\text{s}^{-1}$	$\Delta H_{\text{ox1}}^\ddagger/\text{kJ mol}^{-1}$	$\Delta S_{\text{ox1}}^\ddagger/\text{J K}^{-1} \text{mol}^{-1}$	$\Delta V_{\text{ox1}}^\ddagger/\text{cm}^3 \text{mol}^{-1}$
8.5	70	1.3×10^{-3}	70 ± 7	-90 ± 20	n.d.
4	100	5.1×10^{-4}	80 ± 8	-55 ± 25	n.d.
1.5	90	3.8×10^{-4}	100 ± 15	20 ± 40	-38 ± 4 (pH 2)
0	150	0.62 (293 K)	20 ± 5	-180 ± 20	ca. 0
pH	$K_{\text{OS2}}/\text{M}^{-1}$	$^{298}k_{\text{ox2}}/\text{s}^{-1}$	$\Delta H_{\text{ox2}}^\ddagger/\text{kJ mol}^{-1}$	$\Delta S_{\text{ox2}}^\ddagger/\text{J K}^{-1} \text{mol}^{-1}$	$\Delta V_{\text{ox2}}^\ddagger/\text{cm}^3 \text{mol}^{-1}$
8.5	30	1.8×10^{-4}	90 ± 10	-30 ± 30	n.d.
4	55	2.2×10^{-4}	90 ± 6	-26 ± 20	n.d.
1.5	40	2.0×10^{-4}	100 ± 12	18 ± 40	-41 ± 3 (pH 2)
0	40	1.2×10^{-3} (293 K)	80 ± 10	-20 ± 50	-5.2 ± 0.8

^aThe values of K_{OS} (according to eq 1) are the average from the values at the different temperatures measured.

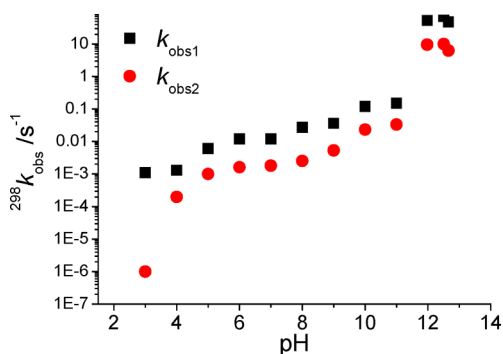
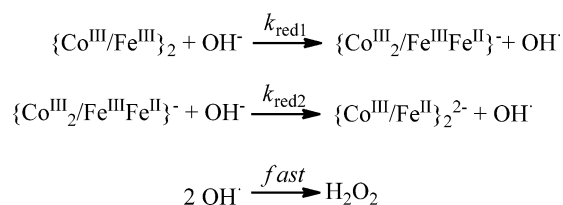


Figure 7. Logarithmic-scale plot of the fast and slow rate constants for the two steps observed upon reduction of the $\{\text{Co}^{\text{III}}/\text{Fe}^{\text{III}}\}_2$ square with OH^- at different buffered pH values at 25°C ($[\text{square}] \approx 4 \times 10^{-4} \text{ M}$; $I = 1.0 \text{ M}$ (NaClO_4)).

of the values k_{obs} obtained under the different conditions of the study, and Scheme 3 collects the reaction sequence that results

Scheme 3



from the data. In this scheme, the values of k_{red1} and k_{red2} necessarily include the two equilibrium constants involving hydroxide, which are in the above-mentioned range.

From the values obtained, it is clear that the validity of the previous oxidation data collected at $\text{pH} > 3$ has to be considered with caution because a faster reduction of the oxidized complex is occurring simultaneously in an approximately catalytic reaction. Probably the observed process corresponds de facto to an oxidation reaction but once the buffer has been consumed.

In this regard, cyclic voltammetry experiments were conducted at variable pH values in the range where a dramatic increase on the reduction rate constants is observed (7–13; Figure 7). The purpose of these measurements was to examine the possible occurrence of an electrochemically catalyzed oxidation of OH^- to H_2O_2 . Figure 8 shows that the fully reduced complex is reversibly oxidized in two discrete steps to the $\{\text{Co}^{\text{III}}/\text{Fe}^{\text{III}}\text{Fe}^{\text{II}}\}^-$ and $\{\text{Co}^{\text{III}}/\text{Fe}^{\text{III}}\}$ complexes at $\text{pH} 7$. However, at higher pH values, the voltammetry is slightly perturbed and the peak oxidative current (i_{pa}) of the first wave increases slightly above $\text{pH} 10$. This behavior is expected for an electrochemical oxidation coupled to a catalytic chemical reaction (Scheme S1) and confirms that hydroxide is only oxidized by $\{\text{Co}^{\text{III}}/\text{Fe}^{\text{III}}\}_2$ at an appreciable rate above $\text{pH} 10$ under the nonbuffered experimental conditions used here. Two clarifications should be noted in relation to Figure 8. First, the nonspecific oxidation of hydroxide by the electrode is only observed at very high potentials ($> 0.85 \text{ V}$ vs NHE) and is not responsible for the change in the peak anodic current (i_{pa}). Second, even though the change in i_{pa} is small, it is definitive; this is indicated by the stable baseline current during the initial

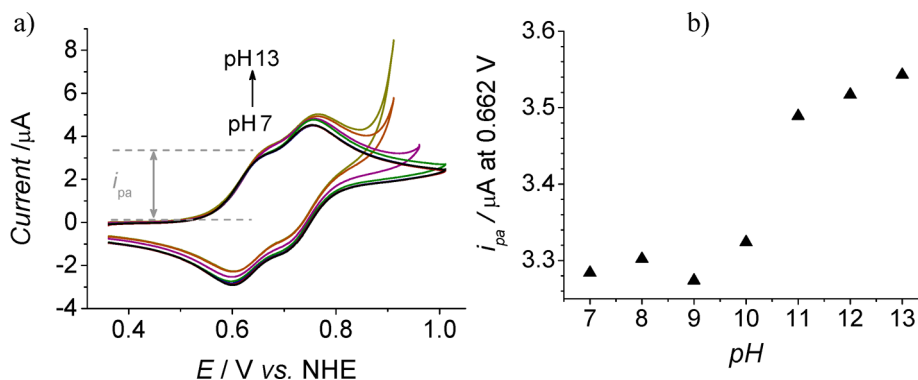


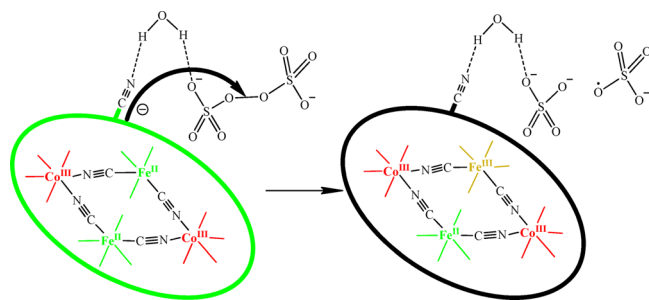
Figure 8. (a) pH-dependent voltammetry of a $7.3 \times 10^{-4} \text{ M}$ solution of $\{\text{Co}^{\text{III}}/\text{Fe}^{\text{II}}\}_2^{2-}$ in H_2O ($I = 0.1 \text{ M}$ LiClO_4 , Scan rate = 10 mV s^{-1}). Potential initially swept in the positive direction. (b) pH dependence of the peak anodic current (i_{pa}) at 0.662 V .

oxidation sweep (i.e., the current at 0.4 V vs NHE is the same across the range of pH values during the initial sweep in the positive direction).

Mechanism of the $\{\text{Co}^{\text{III}}/\text{Fe}^{\text{II}}\}_2^{2-}$ Oxidation Process.

From the data collected, a key difference emerges between the oxidation kinetics of the dianionic $\{\text{Co}^{\text{III}}/\text{Fe}^{\text{II}}\}_2^{2-}$ square complex and the parent monoanionic series of $(\text{Co}^{\text{III}}/\text{Fe}^{\text{II}})^-$ dinuclear species previously reported. While for the mixed-valent monoanionic $(\text{Co}^{\text{III}}/\text{Fe}^{\text{II}})^-$ dinuclear complexes the buildup of outer-sphere precursor complexes with peroxodisulfate (according to eq 1) is minimal, in the present case, the equilibrium constants, K_{OS} , indicated in Scheme 2 are large enough for the observation of limiting kinetics in both consecutive oxidation reaction rate-determining steps (Table 1 and Figure 5).⁴⁴ In the previous studies with the $(\text{Co}^{\text{III}}/\text{Fe}^{\text{II}})^-$ dinuclear species, the only time this behavior was observed was when $[\text{Co}(\text{oxalate})_3]^{3-}$ was used as the oxidant, despite the unfavorable increase in charge repulsion.⁴⁰ This fact was attributed to a solvent-assisted nature of the outer-sphere complex formed, which was also thoroughly described for similar $[\text{Co}(\text{oxalate})_3]^{3-}$ reactivity.⁴⁷ It is thus clear that in the present case an outer-sphere solvent-assisted encounter complex is formed with $\text{S}_2\text{O}_8^{2-}$, both with the dianionic $\{\text{Co}^{\text{III}}/\text{Fe}^{\text{II}}\}_2^{2-}$ and monoanionic $\{\text{Co}^{\text{III}}_2/\text{Fe}^{\text{III}}\text{Fe}^{\text{II}}\}^-$ species, in the first and second rate-determining reaction steps, respectively. Furthermore, the fact that the ox2a and ox2b reaction steps are observed in the oxidation process (Scheme 2), despite the possible operation of reaction oxf2, indicates that the solvent-assisted outer-sphere complex formed in ox1a involves solely one of the oxo groups of peroxodisulfate, thus liberating the resulting $\text{SO}_4^{\bullet-}$ radical to the reaction medium. In this way, a two-electron oxidation process is not operative, and the liberated radical can react with both $\{\text{Co}^{\text{III}}/\text{Fe}^{\text{II}}\}_2^{2-}$ and $\{\text{Co}^{\text{III}}_2/\text{Fe}^{\text{III}}\text{Fe}^{\text{II}}\}^-$, ensuring the observation of the second step (ox2a and ox2b, Scheme 2) of the full process (Scheme 4).

Scheme 4



In this respect, from the data in Table 1, it is also clear that the values of K_{OS} decrease by ca. half upon going from the $\{\text{Co}^{\text{III}}/\text{Fe}^{\text{II}}\}_2^{2-}$ to $\{\text{Co}^{\text{III}}_2/\text{Fe}^{\text{III}}\text{Fe}^{\text{II}}\}^-$ complexes, opposite to that expected considering the electrostatics involved; clearly, some other factor has to be dominant. The only possibility to come to terms with this fact relates precisely again with the existence of a solvent-assisted outer-sphere complexation, where H_2O is more tightly bound to more anionic complexes.^{48–50} Nevertheless, when the fully protonated $\text{H}_2\{\text{Co}^{\text{III}}/\text{Fe}^{\text{II}}\}_2$ species is considered (pH 0), the trend is maintained with equivalent (if not larger) values of K_{OS} , thus implying that the outer-sphere solvent-assisted complexation should occur on the nonprotonated nitrile units; even simultaneous hydrogen bonding between a molecule of H_2O

and the nonprotonated and protonated nitrile units can explain these facts (Schemes 4 and S2).^{51,52}

As for the kinetic and activation parameters at $\text{pH} > 2$ (see Table 1), there is a dramatic change going from the single (pH 1.5–2) to the doubly protonated mixed-valence square complex (pH 0). The first step of the oxidation reaction (k_{ox1}) is accelerated by a factor of 10^3 , while the second reaction rate constant undergoes only a 10-fold increase. These values are clearly related to the thermal activation ΔH^\ddagger and ΔS^\ddagger values, which indicate a much higher degree of association in the transition state and a lower enthalpy demand with decreasing pH (both effects are more pronounced for the first rate-determining step of the oxidation reaction). Interestingly, the redox potential of the Fe centers becomes more positive upon protonation,^{26,30} which would be expected to produce higher enthalpy demands. Again, the proper association of the oxidant and reductant via a solvent molecule should be held responsible for the acceleration found (vide supra); alternatively, direct interaction of the peroxodisulfate anion with protonated nitrile groups could also explain the changes (Scheme S3). As for the volumes of activation, these show trends opposite to those of ΔS^\ddagger , in agreement with the operation of hydrogen-bonding interactions in the transition state, and are mostly related to desolvation of the complexes, as found for similar systems.^{48,49,53}

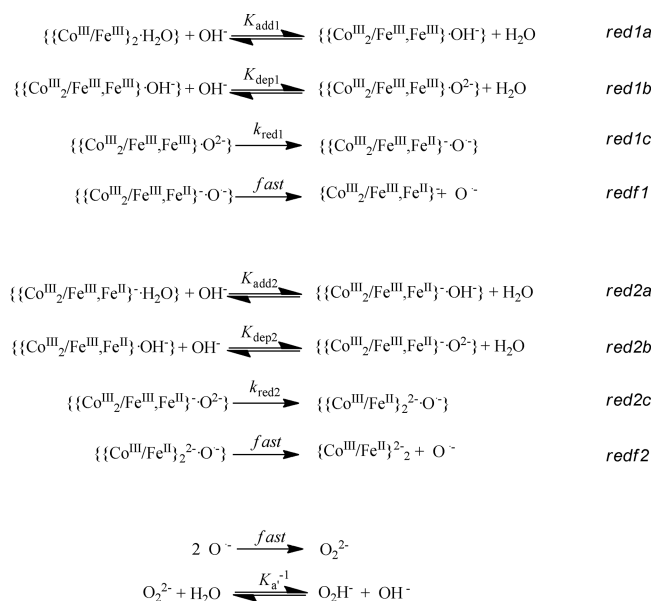
Mechanism of the $\{\text{Co}^{\text{III}}/\text{Fe}^{\text{III}}\}_2$ Reduction Process. The data collected and shown in Figure 7 clearly indicate that, as found in previous studies,^{40,54} even though the reduction potentials do not predict the formation of H_2O_2 ($E^\circ = +1.77$ V), H_2O_2 is formed in a process that appears to be formally endergonic. In any case, the reactivity of the iron hexacyanido/ H_2O_2 redox system is strongly dependent on the counterions, pH, light, and reaction medium.^{55,56} Most of the processes lead to decomposition of H_2O_2 or photochemical degradation of the hexacyanido complexes to produce Prussian-blue-type compounds. We have not observed this type of degradation on our samples; furthermore, most of the Fe^{II} oxidations by H_2O_2 processes involve the coordination of a hydroperoxide anion to a substitutionally active complex, which is not the case in the system that we are dealing with here. There must be some sort of stabilization of the peroxide in our systems, probably related to adduct formation similar to that producing hydrolysis of the cyanido ligands in other systems.

Interestingly, although the redox potential of the Fe center increases with decreasing pH, the trend observed for the rate constants measured for both reaction steps (Scheme 3) is opposite. The previously studied similar reactions on $(\text{Co}^{\text{III}}/\text{Fe}^{\text{III}})$ dinuclear complexes^{40,54} indicated that the formation of an outer-sphere OH^- aggregate and its further deprotonation by a second OH^- group agree with the data obtained; a $[\text{OH}^-]^2$ dependence was observed for the values of k_{obs} . In the present study, such a trend is not observed and, although in the pH range between 5 and 10 the increases of both k_{red1} and k_{red2} are practically linear, the values increase dramatically upon going to pH 11 to reach a final plateau. Increasing the acidity to pH 3 produces an opposite immediate decrease of the second-step rate constant and a buildup of the $\{\text{Co}^{\text{III}}_2/\text{Fe}^{\text{III}}\text{Fe}^{\text{II}}\}^-$ intermediate complex; a further increase in the acidity makes both reduction processes too slow to be observed.

From these data, it is clear that outer-sphere involvement of OH^- with the oxidized $\{\text{Co}^{\text{III}}/\text{Fe}^{\text{III}}\}_2$ square complex plays a crucial role in its reduction to the mixed-valence parent species

and the formation of H_2O_2 . In this respect, it is interesting to note that the aggregation of hydroxide with the reduced $\{\text{Co}^{\text{III}}/\text{Fe}^{\text{II}}\}_2^{2-}$ has already been established by UV–vis spectroscopy.²⁶ Furthermore, the pH values for which dramatic changes in the rate constants are observed can be easily associated with the deprotonation of a coordinated H_2O molecule ($\text{p}K_{\text{a}}$ values of around 3–5) or of a coordinated hydroxide ($\text{p}K_{\text{a}}$ values of around 9–12).⁵⁷ With all of these facts in mind, we propose the reaction sequence shown in Scheme 5 as responsible for the trends observed. From the

Scheme 5



data in Figure 7, the values of both $\text{p}K_{\text{dep1}}$ and $\text{p}K_{\text{dep2}}$ are found to be equivalent and within the 11–12 range; as expected, because of the fact that the values of K_{dep} are directly associated with the deprotonation of a $\{\{\text{Co}^{\text{III}}/\text{Fe}^{\text{III}}\}_2\cdot\text{OH}^-\}$ adduct in reactions red1a and red2b (Scheme 5). Furthermore, compound $\{\{\text{Co}^{\text{III}}/\text{Fe}^{\text{III}}\}_2\cdot\text{H}_2\text{O}\}$ is expected to be more acidic than $\{\{\text{Co}^{\text{III}}_2/\text{Fe}^{\text{III}}_2\}\cdot\text{H}_2\text{O}\}$, as is effectively shown by the value of K_{add} ($\text{p}K_{\text{add1}}$ being one unit lower than $\text{p}K_{\text{add2}}$; 2–3 versus 3–4). As a whole, the process is rather similar to the one established for oxidation of the dinuclear ($\text{Co}^{\text{III}}/\text{Fe}^{\text{II}}$) parent mixed-valence complexes. For the present complexes, though, the higher acidity of the initial $\{\{\text{Co}^{\text{III}}/\text{Fe}^{\text{III}}\}_2\}$ oxidized square allows for full dissociation of the initial adduct, even at high pH. Furthermore, the difference between the acidities of $\{\{\text{Co}^{\text{III}}/\text{Fe}^{\text{III}}\}_2\cdot\text{H}_2\text{O}\}$ and $\{\{\text{Co}^{\text{III}}_2/\text{Fe}^{\text{III}}_2\}\cdot\text{OH}^-\}$ (or the half-reduced intermediate species) allows for a full separation of the effects of K_{add} and K_{dep} for the reaction sequence indicated in Scheme 5.

CONCLUSIONS

The structure of the heterotetranuclear cyanido-bridged square-shaped $[\{\{\text{Co}^{\text{III}}\{(\text{Me})_2(\mu\text{-ET})\text{cyclen}\}\}_2\{(\mu\text{-NC})_2\text{Fe}^{\text{II}}(\text{CN})_4\}_2\}]^{2-}$ mixed-valence complex has been unambiguously established by X-ray diffraction (XRD); the structure shows extensive hydrogen-bonding interactions with H_2O molecules, H_3O^+ , and the N atoms of the terminal cyanido ligands. Spectroelectrochemical measurements indicate that the stability of the complex, as well as those of their partially ($\{\text{Co}_2^{\text{III}}/\text{Fe}^{\text{III}}\text{Fe}^{\text{II}}\}^-$) and fully ($\{\text{Co}^{\text{III}}/\text{Fe}^{\text{III}}\}$) oxidized

counterparts are remarkable, in accordance with the absence of hysteresis observed in these measurements. DFT calculations have also been conducted, and the results agree with the surprising stability and robustness of the $\{\text{Co}^{\text{III}}\text{Fe}^{\text{II}}\}_2^{2-}$ square complex core in any of its oxidized forms. In this respect, MEP maps support the establishment of hydrogen bonds between H_2O and the terminal cyanido ligands. In all, the remarkable robustness displayed opens up the possibility of studying its participation in a wide range of chemical processes in aqueous solution.

In this respect, the kineticomechanistic study of the two-step sequential oxidation reaction of the $\{\text{Co}^{\text{III}}/\text{Fe}^{\text{II}}\}_2^{2-}$ square with peroxodisulfate features a striking difference with the previously reported oxidation reaction of monoanionic ($\text{Co}^{\text{III}}/\text{Fe}^{\text{II}}$)⁻ dinuclear species. For the oxidation reaction of this anionic tetranuclear square-shaped complex, the actuation of an outer-sphere H_2O -assisted encounter complex involving an oxo group of the peroxodisulfate anion is evident. The activation parameters are in agreement with the existence of these hydrogen-bonding interactions in the transition state.

Reduction by H_2O of the fully oxidized $\{\text{Co}^{\text{III}}/\text{Fe}^{\text{III}}\}_2$ square, producing H_2O_2 , occurs even at acidic pH values and, according to the interpretation of the kineticomechanistic results obtained, requires the existence of two equilibrium processes prior to the rate-determining step. These involve the existence of an OH^- adduct, with either $\{\text{Co}_2^{\text{III}}/\text{Fe}^{\text{III}}\text{Fe}^{\text{II}}\}^-$ or $\{\text{Co}^{\text{III}}/\text{Fe}^{\text{III}}\}$, and its subsequent deprotonation by another OH^- before the rate-determining generation of H_2O_2 .

Clearly, a fine-tuning of the building block redox potentials via ligand design should expand the current study to further chemically robust polynuclear mixed-valence compounds. This robustness, with the goal being including that of the Co^{III} centers upon reduction, should provide discrete polynuclear molecules with very interesting electron-transfer properties.

EXPERIMENTAL SECTION

General Procedures. The $\{\text{Co}^{\text{III}}/\text{Fe}^{\text{II}}\}_2^{2-}$ square mixed-valence compound was prepared following the procedures already described in the literature;²⁶ UV–vis, inductively coupled plasma mass spectrometry, and cyclic voltammetry were used as characterization techniques.

A solution of the above complex in 1.0 M HClO_4 , followed by long-standing in a refrigerator, produced some aggregates of XRD-quality crystals.

Buffer solutions were prepared using the standard procedures for $3.0 > \text{pH} < 11$; out of that range, HClO_4 or NaOH solutions were used. In all cases, the concentration of the buffer was at least 10-fold that of the reactants and the ionic strength was set at 1.0 with NaClO_4 .^{58,59}

Detection of H_2O_2 after reduction of the $\{\text{Co}^{\text{III}}/\text{Fe}^{\text{III}}\}_2$ oxidized square, was carried out using Quantofix peroxide test sticks (Peroxid 25 from Sigma-Aldrich) at pH 7.3. Blank experiments in the presence of free $\text{S}_2\text{O}_8^{2-}$ or solutions of the initial $\{\text{Co}^{\text{III}}/\text{Fe}^{\text{II}}\}_2^{2-}$ square mixed-valence compound showed no presence of H_2O_2 .

DFT Calculations. All DFT calculations were carried out using H_2O as the solvent (PCM, see below) with the *Gaussian09* (revision D.01)⁶⁰ electronic structure package with a 10^{-8} convergence criterion for the density matrix elements, using the hybrid functional B3LYP.^{61–63} The standard 6-31G* basis set^{64–66} was used for all H, C, N, and O atoms, while the Stuttgart basis set (SDD),^{64,67} including the associated effective core potential to describe the core electrons, was employed for the Fe and Co atoms. Ultrafine integration grids were used in all calculations to ensure a satisfactory convergence. In all cases, the solvation energies were computed in H_2O with the (IEF-PCM) continuum dielectric solvation model^{68,69} using the SMD radii and nonelectrostatic terms. The dispersion correction terms⁷⁰ were

included in all of the calculations by using the D3 method of Grimme et al.⁷¹ Vibrational analysis was performed for all of the computed structures to ensure the nature of the stationary, which have zero imaginary frequencies.

X-ray Structure Analysis. A caramel prismatic specimen of $C_{36}H_{74}Cl_4Co_2Fe_2N_{20}O_{27}$, approximate dimensions 0.178 mm \times 0.198 mm \times 0.477 mm, was used for X-ray crystallographic analysis. The X-ray intensity data were measured on a D8 Venture system equipped with a multilayer monochromator and a Mo microfocus ($\lambda = 0.71073$ Å). The frames were integrated with the Bruker S $AINT$ software package⁷² using a narrow-frame algorithm. The integration of the data using a monoclinic unit cell yielded a total of 126114 reflections to a maximum θ angle of 30.58° (0.70 Å resolution), of which 9844 were independent (average redundancy 12.811, completeness = 99.6%, $R_{int} = 5.80\%$, and $R_{sig} = 2.83\%$) and 8040 (81.67%) were greater than $2\sigma(F^2)$. The final cell constants of $a = 28.454(6)$ Å, $b = 10.644(2)$ Å, $c = 21.226(4)$ Å, $\alpha = 90.00(3)^\circ$, $\beta = 91.14(3)^\circ$, $\gamma = 90.00(3)^\circ$, and volume = 6427(2) Å³ are based upon refinement of the XYZ centroids of reflections above $20\sigma(I)$. Data were corrected for absorption effects using the multiscan method (SADABS).⁷³ The calculated minimum and maximum transmission coefficients (based on the crystal size) are 0.6550 and 0.7461.

The structure was solved and refined using the Bruker SHELXTL software package⁷⁴ using the space group $C12/c1$, with $Z = 4$ for the formula unit $C_{36}H_{74}Cl_4Co_2Fe_2N_{20}O_{27}$. The final anisotropic full-matrix least-squares refinement on F^2 with 446 variables converged at $R1 = 6.42\%$ for the observed data and $wR2 = 7.10\%$ for all data. The goodness-of-fit was 1.121. The largest peak in the final difference electron density synthesis was $1.580 e^- \text{Å}^{-3}$, and the largest hole was $-1.945 e^- \text{Å}^{-3}$ with a root-mean-square deviation of $0.132 e^- \text{Å}^{-3}$. On the basis of the final model, the calculated density was $1.644 g \text{cm}^{-3}$ and $F(000) 3280 e^-$. Table S3 collects the relevant data for the diffraction.

Electrochemistry. Electrochemistry experiments were carried out with a BioLogic SP-150 instrument using a glassy carbon working electrode, a Ag/AgCl (3 M KCl) reference electrode, and a platinum wire counter electrode on 1×10^{-3} M solutions of the sample and using 0.1 M NaClO₄ as the supporting electrolyte, unless otherwise stated.

Spectroelectrochemistry experiments were carried out with the same instrument and the same standard setup in a CHI cell in a HP8453 UV–vis spectrophotometer.

Kinetics. The kinetic profiles for the reactions at ambient pressure were followed by UV–vis spectroscopy in the 700–300 nm range on HP8452A or Cary 50 instruments equipped with thermostated multicell transport. Runs with $t_{1/2} < 10$ s were performed using an Applied Photophysics SX20 MV stopped-flow instrument with photodiode-array detection (J&M TIDAS). For runs carried out at elevated pressures with $t_{1/2} > 10$ s, an already-described pressurizing cell system setup connected to a TIDAS J&M instrument was used.⁴⁸ For experiments run at variable pressure with $t_{1/2} < 10$ s, a previously described pressurized stopped-flow mixing unit connected with fiber optics to a J&M TIDAS instrument was used.⁷⁵

The observed rate constants were derived from absorbance versus time traces at the wavelengths where a maximum increase and/or decrease of the absorbance were observed. Calculation of the observed rate constants from absorbance versus time monitoring of the reactions, studied under first-order concentration conditions, was carried out using the *Specfit* or *ReactLab* software packages;^{41,42} the general kinetic technique is that previously described.^{40,76} All post-run fittings were carried out by the standard available commercial programs.

For the oxidation reactions, solutions of the square compound were prepared in the relevant buffers at $I = 1.0$ M (NaClO₄) and mixed with the relevant amounts of a peroxodisulfate-buffered ($I = 1.0$ M NaClO₄) stock solution and buffer at $I = 1.0$ M NaClO₄. For the reduction process, the oxidized square was dissolved in 0.001 M HClO₄, and this was added to the relevant buffered solutions for the study ($I = 1.0$ M NaClO₄).

■ ASSOCIATED CONTENT

● Supporting Information

The Supporting Information is available free of charge on the ACS Publications website at DOI: 10.1021/acs.inorgchem.8b01147.

Values of observed rate constants, crystal data structure refinement, stacking of the anionic squares of the $\{Co^{III}/Fe^{II}\}_2^{2-}$ complex, potential speciation plot, time-resolved and *Specfit*-calculated spectra, and additional schemes (PDF)

Accession Codes

CCDC 1827523 contains the supplementary crystallographic data for this paper. These data can be obtained free of charge via www.ccdc.cam.ac.uk/data_request/cif, or by emailing data_request@ccdc.cam.ac.uk, or by contacting The Cambridge Crystallographic Data Centre, 12 Union Road, Cambridge CB2 1EZ, UK; fax: +44 1223 336033.

■ AUTHOR INFORMATION

Corresponding Author

*E-mail: manel.martinez@qi.ub.es.

ORCID

Paul V. Bernhardt: 0000-0001-6839-1763

Montserrat Ferrer: 0000-0002-4034-2596

Jesús Jover: 0000-0003-3383-4573

Manuel Martínez: 0000-0002-6289-4586

Notes

The authors declare no competing financial interest.

■ ACKNOWLEDGMENTS

Financial support from the Spanish Ministerio de Economía y Competitividad (CTQ2015-65707C2-1/FEDER) is acknowledged.

■ REFERENCES

- (1) Vardhan, H.; Yusubov, M.; Verpoort, F. Self-assembled metal-organic polyhedra: An overview of various applications. *Coord. Chem. Rev.* **2016**, *306*, 171–194.
- (2) Zarra, S.; Wood, D. M.; Roberts, D. A.; Nitschke, J. R. Molecular containers in complex chemical systems. *Chem. Soc. Rev.* **2015**, *44*, 419–432.
- (3) Chakrabarty, R.; Mukherjee, P. S.; Stang, P. J. Supramolecular Coordination: Self-Assembly of Finite Two- and Three-Dimensional Ensembles. *Chem. Rev.* **2011**, *111*, 6810–6918.
- (4) Amijs, C. H. M.; van Klink, G. P. M.; van Koten, G. Metallasupramolecular architectures, an overview of functional properties and applications. *Dalton Trans.* **2006**, 308–327.
- (5) Croue, V.; Goeb, S.; Salle, M. Metal-driven self-assembly: the case of redox-active discrete architectures. *Chem. Commun.* **2015**, *51*, 7275–7289.
- (6) Beer, P. D.; Berry, N.; Drew, M. G. B.; Fox, O. D.; Padilla-Tosta, M. E.; Patell, S. Self-assembled dithiocarbamate-copper(II) macrocycles for electrochemical anion recognition. *Chem. Commun.* **2001**, 199–200.
- (7) Fabrizi de Biani, F.; Corsini, M.; Zanello, P.; Yao, H.; Bluhm, M. E.; Grimes, R. N. Electronic Properties of Mononuclear, Dinuclear, and Polynuclear Cobaltacarboranes: Electrochemical and Spectroelectrochemical Studies. *J. Am. Chem. Soc.* **2004**, *126*, 11360–11369.
- (8) Chifotides, H. T.; Giles, I. D.; Dunbar, K. R. Supramolecular Architectures with π -Acidic 3,6-Bis(2-pyridyl)-1,2,4,5-tetrazine Cavities: Role of Anion- π Interactions in the Remarkable Stability of Fe(II) Metallacycles in Solution. *J. Am. Chem. Soc.* **2013**, *135*, 3039–3055.

- (9) Chisholm, M. H.; Patmore, N. J.; Reed, C. R.; Singh, N. Oxalate Bridged Triangles Incorporating Mo_2^{4+} Units. Electronic Structure and Bonding. *Inorg. Chem.* **2010**, *49*, 7116–7122.
- (10) Matsumoto, T.; Newton, G. N.; Shiga, T.; Hayami, S.; Matsui, Y.; Okamoto, H.; Kumai, R.; Murakami, Y.; Oshio, H. Programmable spin-state switching in a mixed-valence spin-crossover iron grid. *Nat. Commun.* **2014**, *5*, 3865.
- (11) Aguila, D.; Prado, Y.; Koumoussi, E. S.; Mathoniere, C.; Clerac, R. Switchable Fe/Co Prussian blue networks and molecular analogues. *Chem. Soc. Rev.* **2016**, *45*, 203–224.
- (12) Berlinguette, C. P.; Dragulescu-Andrasi, A.; Sieber, A.; Güdel, H. U.; Achim, C.; Dunbar, K. R. A Charge-Transfer-Induced Spin Transition in a Discrete Complex: The Role of Extrinsic Factors in Stabilizing Three Electronic Isomeric Forms of a Cyanide-Bridged Co/Fe Cluster. *J. Am. Chem. Soc.* **2005**, *127*, 6766–6779.
- (13) Shatruck, M.; Dragulescu-Andrasi, A.; Chambers, K. E.; Stoian, S. A.; Bominaar, E. L.; Achim, C.; Dunbar, K. R. Properties of Prussian Blue Materials Manifested in Molecular Complexes: Observation of Cyanide Linkage Isomerism and Spin-Crossover Behavior in Pentanuclear Cyanide Clusters. *J. Am. Chem. Soc.* **2007**, *129*, 6104–6116.
- (14) Nihei, M.; Ui, M.; Hoshino, N.; Oshio, H. Cyanide-Bridged Iron(II,III) Cube with Multisteped Redox Behavior. *Inorg. Chem.* **2008**, *47*, 6106–6108.
- (15) Li, D.; Clérac, R.; Roubeau, O.; Harté, E.; Mathonière, C.; Le Bris, R.; Holmes, S. M. Magnetic and Optical Bistability Driven by Thermally and Photoinduced Intramolecular Electron Transfer in a Molecular Cobalt-Iron Prussian Blue Analogue. *J. Am. Chem. Soc.* **2008**, *130*, 252–258.
- (16) Mondal, A.; Li, Y.; Herson, P.; Seuleiman, M.; Boillot, M. L.; Riviere, E.; Julve, M.; Rechinat, L.; Bousseksou, A.; Lescouezec, R. Photomagnetic effect in a cyanide-bridged mixed-valence $\{\text{Fe}^{\text{II}}_2\text{Fe}^{\text{III}}_2\}$ molecular square. *Chem. Commun.* **2012**, *48*, 5653–5655.
- (17) Zheng, C.; Xu, J.; Wang, F.; Tao, J.; Li, D. Spin crossover and reversible single-crystal to single-crystal transformation behaviour in two cyanide-bridged mixed-valence $\{\text{Fe}^{\text{III}}_2\text{Fe}^{\text{II}}_2\}$ clusters. *Dalton Trans.* **2016**, *45*, 17254–17263.
- (18) Nihei, M.; Yanai, Y.; Hsu, I. J.; Sekine, Y.; Oshio, H. A Hydrogen-Bonded Cyanide-Bridged $[\text{Co}_2\text{Fe}_2]$ Square Complex Exhibiting a Three-Step Spin Transition. *Angew. Chem., Int. Ed.* **2017**, *56*, 591–594.
- (19) De, S.; Jimenez, J. R.; Li, Y.; Chamoreau, L. M.; Flambard, A.; Journaux, Y.; Bousseksou, A.; Lescouezec, R. One synthesis: two redox states. Temperature-oriented crystallization of a charge transfer $\{\text{Fe}_2\text{Co}_2\}$ square complex in a $\{\text{Fe}^{\text{II}}_{\text{LS}}\text{Co}^{\text{III}}_{\text{LS}}\}_2$ diamagnetic or $\{\text{Fe}^{\text{III}}_{\text{LS}}\text{Co}^{\text{II}}_{\text{HS}}\}_2$ paramagnetic state. *RSC Adv.* **2016**, *6*, 17456–17459.
- (20) Zhang, Y. Z.; Ferko, P.; Siretanu, D.; Ababei, R.; Rath, N. P.; Shaw, M. J.; Clérac, R.; Mathonière, C.; Holmes, S. M. Thermochemical and Photoresponsive Cyanometalate Fe/Co Squares: Toward Control of the Electron Transfer Temperature. *J. Am. Chem. Soc.* **2014**, *136*, 16854–16864.
- (21) Cao, L.; Tao, J.; Gao, Q.; Liu, T.; Xia, Z.; Li, D. Selective on/off switching at room temperature of a magnetic bistable $\{\text{Fe}_2\text{Co}_2\}$ complex with single crystal-to-single crystal transformation via intramolecular electron transfer. *Chem. Commun.* **2014**, *50*, 1665–1667.
- (22) Siretanu, D.; Li, D.; Buisson, L.; Bassani, D. M.; Holmes, S. M.; Mathoniere, C.; Clérac, R. Controlling Thermally Induced Electron Transfer in Cyano-Bridged Molecular Squares: From Solid State to Solution. *Chem. - Eur. J.* **2011**, *17*, 11704–11708.
- (23) Nihei, M.; Sekine, Y.; Suganami, N.; Nakazawa, K.; Nakao, A.; Nakao, H.; Murakami, Y.; Oshio, H. Controlled Intramolecular Electron Transfers in Cyanide-Bridged Molecular Squares by Chemical Modifications and External Stimuli. *J. Am. Chem. Soc.* **2011**, *133*, 3592–3600.
- (24) Mercuriol, J.; Li, Y.; Pardo, E.; Risset, O.; Seuleiman, M.; Rousseliere, H.; Lescouezec, R.; Julve, M. $[\text{Fe}^{\text{II}}_{\text{LS}}\text{Co}^{\text{III}}_{\text{LS}}]_2$ [Left-right arrow] $[\text{Fe}^{\text{III}}_{\text{LS}}\text{Co}^{\text{II}}_{\text{HS}}]_2$ photoinduced conversion in a cyanide-bridged heterobimetallic molecular square. *Chem. Commun.* **2010**, *46*, 8995–8997.
- (25) Nihei, M.; Sekine, Y.; Suganami, N.; Oshio, H. Thermally Two-stepped Spin Transitions Induced by Intramolecular Electron Transfers in a Cyanide-bridged Molecular Square. *Chem. Lett.* **2010**, *39*, 978–979.
- (26) Alcázar, L.; Aullón, G.; Ferrer, M.; Martínez, M. Redox-Assisted Self-Assembly of a Water-Soluble Cyanido-Bridged Mixed Valence $\{\text{Co}^{\text{III}}/\text{Fe}^{\text{II}}\}_2$ Square. *Chem. - Eur. J.* **2016**, *22*, 15227–15230.
- (27) Bernhardt, P. V.; Martínez, M. The First Structurally Characterized Discrete Dinuclear μ -Cyano Hexacyanoferrate Complex. *Inorg. Chem.* **1999**, *38*, 424–425.
- (28) Bernhardt, P. V.; Macpherson, B. P.; Martínez, M. Discrete Dinuclear Cyano-Bridged Complexes. *Inorg. Chem.* **2000**, *39*, 5203–5208.
- (29) Bernhardt, P. V.; Bozoglian, F.; Macpherson, B. P.; Martínez, M. Tuning the metal to metal charge transfer energy of cyano-bridged dinuclear complexes. *Dalton Trans.* **2004**, 2582–2587.
- (30) Bernhardt, P. V.; Bozoglian, F.; Macpherson, B. P.; Martínez, M. Molecular mixed-valence cyanide bridged $\text{Co}^{\text{III}}\text{Fe}^{\text{II}}$ complexes. *Coord. Chem. Rev.* **2005**, *249*, 1902–1916.
- (31) Bernhardt, P. V.; Bozoglian, F.; González, G.; Martínez, M.; Macpherson, B. P.; Sienna, B. Dinuclear Cyano-Bridged $\text{Co}^{\text{III}}/\text{Fe}^{\text{II}}$ Complexes as Precursors for Molecular Mixed Valence Complexes of Higher Nuclearity. *Inorg. Chem.* **2006**, *45*, 74–82.
- (32) Bernhardt, P. V.; Martínez, M.; Rodríguez, C. Molecular $\text{Co}^{\text{III}}/\text{Fe}^{\text{II}}$ Cyano-Bridged Mixed-Valence Compounds with High Nuclearities and Diversity of Co^{III} Coordination Environments: Preparative and Mechanistic Aspects. *Inorg. Chem.* **2009**, *48*, 4787–4797.
- (33) Bernhardt, P. V.; Martínez, M.; Rodríguez, C. Outer-Sphere Redox Reactions leading to the Formation of Discrete $\text{Co}^{\text{III}}/\text{Fe}^{\text{II}}$ pyrazine-Bridged Mixed Valence Compounds. *Eur. J. Inorg. Chem.* **2010**, *2010*, 562–569.
- (34) Bernhardt, P. V.; Martínez, M.; Rodríguez, C.; Vazquez, M. Discrete $\text{Rh}^{\text{III}}/\text{Fe}^{\text{II}}$ and $\text{Rh}^{\text{III}}/\text{Fe}^{\text{II}}/\text{Co}^{\text{III}}$ Cyanide-Bridged Mixed Valence Compounds. *Inorg. Chem.* **2011**, *50*, 1429–1440.
- (35) Oshio, H.; Onodera, H.; Tamada, O.; Mizutani, H.; Hikichi, T.; Ito, T. Cyanide-Bridged Fe-Fe and Fe-Co Molecular Squares: Structures and Electrochemistry of $[\text{Fe}^{\text{II}}_4(\mu\text{-CN})_4(\text{bpy})_8](\text{PF}_6)_4 \cdot 4\text{H}_2\text{O}$, $[\text{Fe}^{\text{II}}_2\text{Co}^{\text{II}}_2(\mu\text{-CN})_4(\text{bpy})_8](\text{PF}_6)_4 \cdot \text{CHCl}_3 \cdot 2\text{CH}_3\text{CN}$, and $[\text{Fe}^{\text{II}}_2\text{Co}^{\text{III}}_2(\mu\text{-CN})_4(\text{bpy})_8](\text{PF}_6)_6 \cdot 2\text{CHCl}_3 \cdot 4\text{CH}_3\text{NO}_2$. *Chem. - Eur. J.* **2000**, *6*, 2523–2530.
- (36) King, P.; Maeder, M. *Reactlab Redox*; J Plus Consulting Pty Ltd: Western Australia, 2014.
- (37) Zheng, C.; Xu, J.; Yang, Z.; Tao, J.; Li, D. Factors Impacting Electron Transfer in Cyano-Bridged $\{\text{Fe}_2\text{Co}_2\}$ Clusters. *Inorg. Chem.* **2015**, *54*, 9687–9689.
- (38) Bard, A. J.; Faulkner, L. R. *Electrochemical Methods: Fundamentals and Applications*; Wiley: Chicago, IL, 2001.
- (39) Bernhardt, P. V.; Bozoglian, F.; Macpherson, B. P.; Martínez, M.; González, G.; Sienna, B. Discrete cyanide bridged mixed-valence Co/Fe complexes: outer sphere redox behaviour. *Eur. J. Inorg. Chem.* **2003**, *2003*, 2512–2518.
- (40) Bernhardt, P. V.; Bozoglian, F.; Macpherson, B. P.; Martínez, M.; Merbach, A. E.; González, G.; Sienna, B. Oxidation of Mixed-Valence $\text{Co}^{\text{III}}/\text{Fe}^{\text{II}}$ Complexes Reversed at High pH: A Kinetic-Mechanistic Study of Water Oxidation. *Inorg. Chem.* **2004**, *43*, 7187–7195.
- (41) Maeder, M.; King, P. *ReactLab*; Jplus Consulting Pty Ltd.: East Fremantle, Australia, 2009.
- (42) Binsted, R. A.; Zuberbuhler, A. D.; Jung, B. *SPECFIT32 [3.0.34]*; Spectrum Software Associates: Marlborough, MA, 2005.
- (43) Espenson, J. H. *Chemical Kinetics and Reaction Mechanisms*; McGraw-Hill: New York, 1981.
- (44) Lippin, A. G. *Redox Mechanisms in Inorganic Chemistry*; Ellis Horwood: Chichester, U.K., 1994.
- (45) Tobe, M. L.; Burgess, J. *Inorganic Reaction Mechanisms*; Longman: New York, 1999.

- (46) Ducommun, Y.; Merbach, A. E. *Inorganic High Pressure Chemistry*; Elsevier: Amsterdam, The Netherlands, 1986; pp 69–114.
- (47) Geselowitz, D. A.; Hammershoi, A.; Taube, H. Stereoselective electron transfer reactions of (ethylenediaminetetraacetato)cobaltate(III), (propylenediaminetetraacetato)cobaltate(III) and (1,2-cyclohexanediaminetetraacetato)cobaltate(III) with tris(ethylenediamine)cobalt(II). *Inorg. Chem.* **1987**, *26*, 1842–1845.
- (48) Martínez, M.; Pitarque, M. A.; van Eldik, R. Outer-sphere redox reactions in sterically hindered pentaam(m)inecobalt(III) complexes. A temperature and pressure dependence kinetic study. *J. Chem. Soc., Dalton Trans.* **1994**, 3159–3163.
- (49) Martínez, M.; Pitarque, M. A.; van Eldik, R. Outer-sphere redox reactions of $[\text{Co}^{\text{III}}(\text{NH}_3)_5(\text{H}_2\text{P}_2\text{O}_7)]^{(m-3)-}$ complexes. A temperature- and pressure-dependence kinetic study on the influence of the phosphorus oxoanions. *J. Chem. Soc., Dalton Trans.* **1996**, 2665–2671.
- (50) Bernhardt, P. V.; González, M. A.; Martínez, M. Kinetic-mechanistic Study on the Oxidation of Biologically Active Iron(II) Bis(thiosemicarbazone) Complexes by Air. Importance of NH-O₂ Interactions As Established by Activation Volumes. *Inorg. Chem.* **2017**, *56*, 14284–14290.
- (51) Basha, M. T.; Bordini, J.; Richardson, D. E.; Martínez, M.; Bernhardt, P. V. Kinetic-mechanistic Studies on Methemoglobin Generation by Biologically Active Thiosemicarbazone Iron(III) Complexes. *J. Inorg. Biochem.* **2016**, *162*, 326–333.
- (52) Bernhardt, P. V.; Martínez, M.; Rodríguez, C.; Vázquez, M. Biologically Active Thiosemicarbazone Fe Chelators and their Reactions with Ferrioxamine B and Ferric EDTA; a Kinetic Study. *Dalton Trans.* **2012**, *41*, 2122–2130.
- (53) Garcia-Amoros, J.; Stopa, G.; Stochel, G.; van Eldik, R.; Martínez, M.; Velasco, D. Activation volumes for cis-to-trans isomerisation reactions of azophenols: a clear mechanistic indicator? *Phys. Chem. Chem. Phys.* **2018**, *20*, 1286–1292.
- (54) Basallote, M. G.; Bernhardt, P. V.; Calvet, T.; Castillo, C. E.; Font-Bardía, M.; Martínez, M.; Rodríguez, C. Mechanistic aspects of the chemistry of mononuclear Cr^{III} complexes with pendant-arm macrocyclic ligands and formation of discrete Cr^{III}/Fe^{II} and Cr^{III}/Fe^{II}/Co^{III} cyano-bridged mixed valence compounds. *Dalton Trans.* **2009**, 9567–9577.
- (55) Eaton, D. R.; Pankratz, M. The reaction of the hexacyanoferrate(III) ion with hydrogen peroxide. *Can. J. Chem.* **1985**, *63*, 793–797.
- (56) Rabai, G.; Kustin, K.; Epstein, I. R. Systematic design of chemical oscillators. 57. Light-sensitive oscillations in the hydrogen peroxide oxidation of ferrocyanide. *J. Am. Chem. Soc.* **1989**, *111*, 8271–8273.
- (57) Atkins, P.; Overton, T.; Rourke, J.; Weller, M.; Armstrong, F. A. *Inorganic Chemistry*; Oxford University Press, 2006.
- (58) Good, N. E.; Winget, G. D.; Winter, W.; Connolly, T. N.; Izawa, S.; Singh, R. M. M. Hydrogen Ion Buffers for Biological Research. *Biochemistry* **1966**, *5*, 467–477.
- (59) Perrin, D. D. Buffers of Low Ionic Strength for Spectrophotometric pK Determinations. *Aust. J. Chem.* **1963**, *16*, 572–578.
- (60) Frisch, M. J.; et al. *Gaussian09*, revision CD.01; Gaussian Inc.: Wallingford, CT, 2009.
- (61) Becke, A. D. Density-functional thermochemistry. III. The role of exact exchange. *J. Chem. Phys.* **1993**, *98*, 5648–5652.
- (62) Lee, C.; Yang, W.; Parr, R. G. Development of the Colle-Salvetti correlation-energy formula into a functional of the electron density. *Phys. Rev. B: Condens. Matter Mater. Phys.* **1988**, *37*, 785–789.
- (63) Miehlich, B.; Savin, A.; Stoll, H.; Preuss, H. Results obtained with the correlation energy density functionals of Becke and Lee, Yang and Parr. *Chem. Phys. Lett.* **1989**, *157*, 200–206.
- (64) Hariharan, P. C.; Pople, J. A. The influence of polarization functions on molecular orbital hydrogenation energies. *Theoret. Chim. Acta* **1973**, *28*, 213–222.
- (65) Hehre, W. J.; Ditchfield, R.; Pople, J. A. Self-Consistent Molecular-Orbital Methods. XII. An Extended Gaussian-Type Basis for Molecular-Orbital Studies of Organic Molecules. *J. Chem. Phys.* **1972**, *56*, 2257–2261.
- (66) Ditchfield, R.; Hehre, W. J.; Pople, J. A. Self-Consistent Molecular-Orbital Methods. IX. An Extended Gaussian-Type Basis for Molecular-Orbital Studies of Organic Molecules. *J. Chem. Phys.* **1971**, *54*, 724–728.
- (67) Dunning, T. H.; Hay, P. J. *Modern Theoretical Chemistry*; Plenum: New York, 1976; pp 1–28.
- (68) Tannor, D. J.; Marten, B.; Murphy, R.; Friesner, R. A.; Sitkoff, D.; Nicholls, A.; Honig, B.; Ringnalda, M.; Goddard, W. A. Accurate First Principles Calculation of Molecular Charge Distributions and Solvation Energies from Ab Initio Quantum Mechanics and Continuum Dielectric Theory. *J. Am. Chem. Soc.* **1994**, *116*, 11875–11882.
- (69) Marten, B.; Kim, K.; Cortis, C.; Friesner, R. A.; Murphy, R. B.; Ringnalda, M. N.; Sitkoff, D.; Honig, B. New Model for Calculation of Solvation Free Energies: Correction of Self-Consistent Reaction Field Continuum Dielectric Theory for Short-Range Hydrogen-Bonding Effects. *J. Phys. Chem.* **1996**, *100*, 11775–11788.
- (70) Marenich, A. V.; Cramer, C. J.; Truhlar, D. G. Universal Solvation Model Based on Solute Electron Density and on a Continuum Model of the Solvent Defined by the Bulk Dielectric Constant and Atomic Surface Tensions. *J. Phys. Chem. B* **2009**, *113*, 6378–6396.
- (71) Grimme, S.; Antony, J.; Ehrlich, S.; Krieg, H. A consistent and accurate ab initio parametrization of density functional dispersion correction (DFT-D) for the 94 elements H-Pu. *J. Chem. Phys.* **2010**, *132*, 154104.
- (72) SAINT, revision 7.68A; Bruker AXS Inc., 2009.
- (73) Sheldrick, G. M. SADABS, revision 2008/1. Bruker AXS Inc., 2008.
- (74) Sheldrick, G. M. SHELXL. *Acta Crystallogr., Sect. A: Found. Crystallogr.* **2008**, *64*, 112–122.
- (75) Zerk, T. J.; Martínez, M.; Bernhardt, P. V. A Kinetic-Mechanistic Study on Cu^{II} Deactivators Employed in Atom Transfer Radical Polym. Cerization. *Inorg. Chem.* **2016**, *55*, 9848–9857.
- (76) Crespo, M.; Martínez, M.; Nabavizadeh, S. M.; Rashidi, M. Kinetic-mechanistic studies on C-X (X = H, F, Cl, Br, I) bond activation reactions on organoplatinum(II) complexes. *Coord. Chem. Rev.* **2014**, *279*, 115–140.